Te-doped selective-area grown InAs nanowires for superconducting hybrid devices

Pujitha Perla,[1,2,*] Anton Faustmann,[1,2,*] Sebastian Kölling,[3] Patrick Zellekens,[1,2] Russell Deacon,[4] H. Aruni Fonseka,[5]
Jonas Kölzer,[1,2] Yuki Sato,[1,2,6] Ana M. Sanchez,[5] Oussama Moutanabbir,[3] Koji Ishibashi,[4] Detlev Grützmacher,[1,7,2]
Mihail Ion Lepsa,[7,2] and Thomas Schäpers[1,2,†]

[1]*Peter Grünberg Institut (PGI-9), Forschungszentrum Jülich, 52425 Jülich, Germany*
[2]*JARA-Fundamentals of Future Information Technology, Jülich-Aachen Research Alliance, Forschungszentrum Jülich and RWTH Aachen University, 52425 Jülich, Germany*
[3]*Department of Engineering Physics, École Polytechnique de Montréal, C.P. 6079, Succ. Centre-Ville, Montréal, Québec, Canada H3C 3A7*
[4]*RIKEN Center for Emergent Matter Science and Advanced Device Laboratory, 351-0198 Saitama, Japan*
[5]*Department of Physics, University of Warwick, Coventry CV4 7AL, United Kingdom*
[6]*Faculty of Science and Engineering Department of Electronics, Doshisha University, Doshisha University, Kyotanabe, Kyoto 610-0321, Japan*
[7]*Peter Grünberg Institut (PGI-10), Forschungszentrum Jülich, 52425 Jülich, Germany*

(Received 19 October 2021; revised 18 January 2022; accepted 4 February 2022; published 24 February 2022)

Semiconductor nanowires have emerged as versatile components in superconducting hybrid devices for Majorana physics and quantum computing. The transport properties of nanowires can be tuned either by field effect or doping. We investigated a series of InAs nanowires the conductivity of which has been modified by *n*-type doping using tellurium. In addition to electron microscopy studies, the wires were also examined with atomic probe tomography to obtain information about the local incorporation of Te atoms. It was found that the Te atoms mainly accumulate in the core of the nanowire and at the corners of the {110} side facets. The efficiency of *n*-type doping was also confirmed by transport measurements. As a demonstrator hybrid device, a Josephson junction was fabricated using a nanowire as a weak link. The corresponding measurements showed a clear increase of the critical current with increase of the dopant concentration.

DOI: 10.1103/PhysRevMaterials.6.024602

I. INTRODUCTION

InAs nanowires have proven to be suitable constituents for various electronic devices [1–4] and also for studying fundamental quantum physics phenomena in nanoscale structures [5–10]. Recently, InAs nanowires attracted attention by their integration in semiconductor-superconductor hybrid structures. A prominent example is the effort regarding the realization of Majorana fermions for topological quantum computing [11,12]. In addition, InAs nanowires can serve as a weak link in gate-controlled Josephson junctions [13,14] for superconducting qubits such as transmons [15,16] or Andreev level qubits [17].

Due to the Fermi level pinning within the conduction band in InAs, a surface accumulation layer forms naturally [18], ensuring that the nanowire is conductive even without doping. In some cases, however, the ability to control conductivity through doping is desired, e.g., for adjusting the channel conductance in field-effect transistors. Nanowire conductivity has also a major impact on the critical current of Josephson junctions based on InAs nanowires [14]. In this respect it is a crucial design parameter to adjust the Josephson energy in the aforementioned transmon qubits [15,16], as well as for gate-controlled superconducting switches in interference structures [19].

In most cases, Si is employed as an *n*-type dopant in InAs nanowires [20–24]. Using Si doping, densities in the order of 10^{19} cm^{-3} are achieved [21,22]. However, apart from the increase of the carrier concentration in the nanowire, Si doping affects the growth kinetics as well as the nanowire dimensions [21,23]. In GaAs, Te is known as a very effective *n*-type dopant [25–27]. As a group VI element Te shows no amphoteric behavior as it is the case for Si in GaAs. As a matter of fact, Te doping already found its applications in *n*-type doped GaAs nanowires [28–31]. Recently, it was demonstrated that Te is also a very efficient dopant in InAs nanowires [32].

To explore the suitability of Te-doped nanowires in superconductor/nanowire hybrid structures, we have grown a series of nanowires with different doping using selective-area molecular beam epitaxy (MBE). The structural properties are investigated by electron microscopy. Detailed information about the dopant distribution in the nanowires is obtained by atom probe tomography (APT). Electrical transport measurements are performed both at room temperature and at 4 K to determine the doping efficiency. Finally, the properties of the doped nanowires for superconducting hybrid structures are investigated by fabricating and measuring nanowire-based Josephson junctions.

---

[*] These authors contributed equally to this work.
[†] th.schaepers@fz-juelich.de

TABLE I. Growth runs for InAs nanowires: growth run, nominal doping concentration, GaTe cell temperature, As_4 BEP, length, diameter, resistivity, carrier concentration, and field-effect mobility from transport measurements at room temperature [36].

Growth run	Te doping (cm^{-3})	GaTe cell (°C)	As_4 BEP (mbar)	Length (μm)	Diameter (nm)	ρ (Ω cm)	n_{3D} (cm^{-3})	μ_{FE} ($\frac{cm^2}{V s}$)
A	5×10^{17}	420	3×10^{-5}	4–5	100 ± 5	18.4×10^{-3}	$(0.75 \pm 0.23) \times 10^{18}$	187
B	1×10^{18}	437	3×10^{-5}	5–6.5	103 ± 5	n.a.	$(1.15 \pm 0.80) \times 10^{18}$	580
C	5×10^{18}	478	3.5×10^{-5}	3.5–4.5	111 ± 5	4.3×10^{-3}	$(2.76 \pm 2.50) \times 10^{18}$	588
D	1×10^{19}	497	3.5×10^{-5}	4–5	113 ± 3	2.7×10^{-3}	$(9.04 \pm 2.29) \times 10^{18}$	215
E	5×10^{18}	478	2.5×10^{-5}	3.5–5	121 ± 7	10.0×10^{-3}	$(1.27 \pm 0.45) \times 10^{18}$	689
F	2.5×10^{19}	520	2.5×10^{-5}	3.5–5	140 ± 8	1.2×10^{-3}	$(5.86 \pm 2.21) \times 10^{18}$	583

II. GROWTH AND DEVICE FABRICATION

The InAs nanowires were grown by MBE using selective area growth on a Si(111) wafer covered by a 20-nm-thick thermally oxidized SiO_2 layer [33,34]. By means of electron beam lithography, hole arrays with a pitch of 1 μm and hole diameter of 80 nm are patterned. The holes are etched by reactive ion etching to a depth of roughly 16 nm followed by cleaning in piranha solution ($H_2SO_4 : H_2O_2 = 3 : 1$). Immediately before growth, an etching step of 60 s in 1% conc. HF is performed in order to remove the remaining SiO_2 in the holes without damaging the Si(111) surface below.

The InAs nanowires are grown without any catalyst via the vapor-solid mechanism [35]. The tellurium is supplied by a GaTe cell. For the first 10 min, a substrate temperature of 480 °C, an In growth rate of 0.08 μm/h, and an As beam equivalent pressure (BEP) of 4×10^{-5} mbar are used to sustain the nanowire self-seeding. The nanowire growth then proceeds with a lower substrate temperature of 460 °C and In growth rate of 0.03 μm/h. For growth runs A to D the As_4 BEP varied between 3 and 3.5×10^{-5} mbar for 3.5 h depending on the Te-doping concentration to avoid changes in the morphology of the nanowires [32]. Here, the Te concentration has been varied between 5×10^{17} and 1×10^{19} cm^{-3} by varying the GaTe cell temperature between 420 °C and 497 °C based on calibrations conducted on Te-doped GaAs layers via Hall measurements. In addition, two samples were grown with a lower As_4 BEP of 2.5×10^{-5} mbar (growth runs E and F) with a nominal doping of 5×10^{18} and 2.5×10^{19} cm^{-3}, respectively. The parameters of the Te-doped InAs nanowires are summarized in Table I.

For the APT measurements discussed below, we also prepared InAs nanowires with different doping concentrations, which are covered by a 50-nm-thick GaSb shell (cf. Table II). The GaSb shell ensures that all atoms of the cross section of the InAs nanowire are gathered by the APT detector.

TABLE II. Growth runs for InAs/GaSb core/shell nanowires with their corresponding nominal doping concentration and the doping concentration determined by APT.

Growth run	Te doping (cm^{-3})	Te (APT) (cm^{-3})
H	1×10^{18}	$(1.47–1.92) \times 10^{18}$
I	7.5×10^{18}	$(2.45–4.95) \times 10^{18}$
J	2.5×10^{19}	$(0.39–1.38) \times 10^{19}$

Specific devices with ohmic contacts have been fabricated for electrical characterization of InAs nanowires with varying Te-doping levels from growth runs A–F. The nanowires have been transferred mechanically using a clean paper tip to highly doped Si substrates covered by a 200-nm-thick thermal SiO_2 layer in order to provide a global back gate. On top of the SiO_2 layer, metallic contact pads and alignment markers have been placed using optical lithography and lift-off processes. Electrical contacts were defined in a four-terminal configuration by electron beam lithography. The contacts consisted of nonalloyed Ti/Au metal layers of 80 nm and 50 nm thickness, respectively, deposited by electron beam evaporation. An Ar^+ sputtering step of 90 s was included before metallization in order to remove the native oxide and to provide a clean semiconductor surface.

The shunted Josephson junctions were processed with nanowires from growth runs A, B, and D. The AuGe shunt resistor is defined by electron beam lithography. It consists of a 10-nm-thick, 1-μm-wide, and 7-μm-long AuGe stripe with a resistance $R_{shunt} = 80–140\,\Omega$. The InAs nanowires are transferred individually onto a Si substrate containing a 5-nm/10-nm-thick Ti/Pt gate pad covered with a 3-nm/12-nm-thick stack of Al_2O_3/HfO_2. The NbTi electrodes that connect the nanowire with the shunt resistor and the surrounding TiN circuit are fabricated by means of Ar ion milling (∼180 s) and the subsequent sputter deposition of 80 nm NbTi via the dc magnetron. Here, the average junction length is in the range of 100 nm and mainly limited by the e-beam lithography. Junctions were fabricated in the center of the transferred nanowires.

III. RESULTS AND DISCUSSION

A. Nanowire structure

Figure 1(a) shows a scanning electron microscopy (SEM) image of an array of Te-doped (1×10^{18} cm^{-3}) nanowires (growth run B). The yield is about 95%. The image confirms the uniformity of length and diameter. In Figs. 1(b) and 1(c), close-ups of a nanowire from growth runs B and D are shown. Up to a Te concentration of 1×10^{-19} cm^{-3} the nanowires show a hexagonal cross section with {110} facets as well as a comparable diameter of around 110 nm. However, for the nanowires with the highest Te concentration of 2.5×10^{-19} cm^{-3} we observe that diameter increased visibly. Furthermore, as can be clearly seen in Figs. 1(d) and 1(e), the

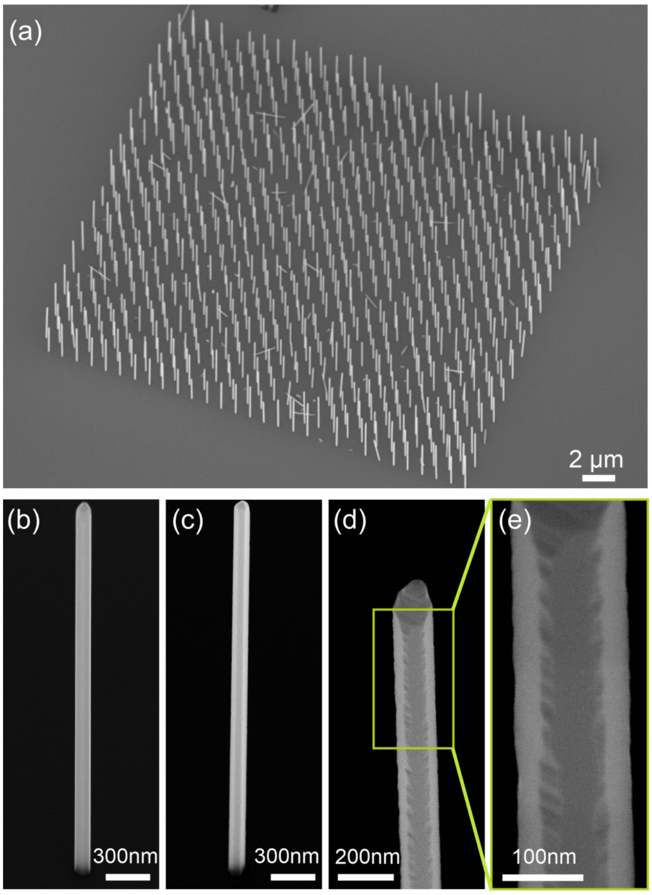

FIG. 1. (a) Scanning electron micrograph of selectively grown Te-doped InAs nanowires with a nominal doping concentration of 1×10^{18} cm^{-3}. The nanowires grow in 80-nm-wide holes with 1 μm pitch. Close-up of nanowires with different Te concentrations: (b) 1×10^{18} cm^{-3} (growth run B), (c) 1×10^{19} cm^{-3} (growth run D), and (d) 2.5×10^{19} cm^{-3} (growth run F), respectively. (e) Zoom-in of (d) showing additional facets forming an irregular dodecagonal shape.

sidewalls of the nanowire developed additional {112} facets, forming an irregular dodecagonal shape.

Tellurium atoms have a surfactant effect accumulating on the side facets and decreasing the diffusion length of the host indium atoms [37–39]. As a result, an increase of the nanowire diameter is expected, which was observed also in our experiments (cf. Table I). A similar behavior has Sb in InAs(Sb) nanowires, where with increasing Sb supply the nanowire radius increases accordingly [40,41].

B. Transmission electron microscopy

The crystal structure of the nanowires from all the growths is mainly formed by the wurtzite (WZ) region containing inclusions of zinc blende (ZB) segments and twining planes, as shown in Fig. 2(a) for a nanowire from growth run C. In contrast to the previous study on randomly positioned Te-doped InAs nanowires [32], in these nanowires, no clear change in crystal structure was observed with the increase of the Te-doping level. Figure 2(b) shows a higher magnification image of the tip of the nanowire. Assuming similar facets are maintained during growth, the top (111) growth facet is of smaller diameter than the rest of the nanowire. Therefore, it can be safely assumed that the nanowire growth takes place by adatom deposition on multiple facets on the tip region.

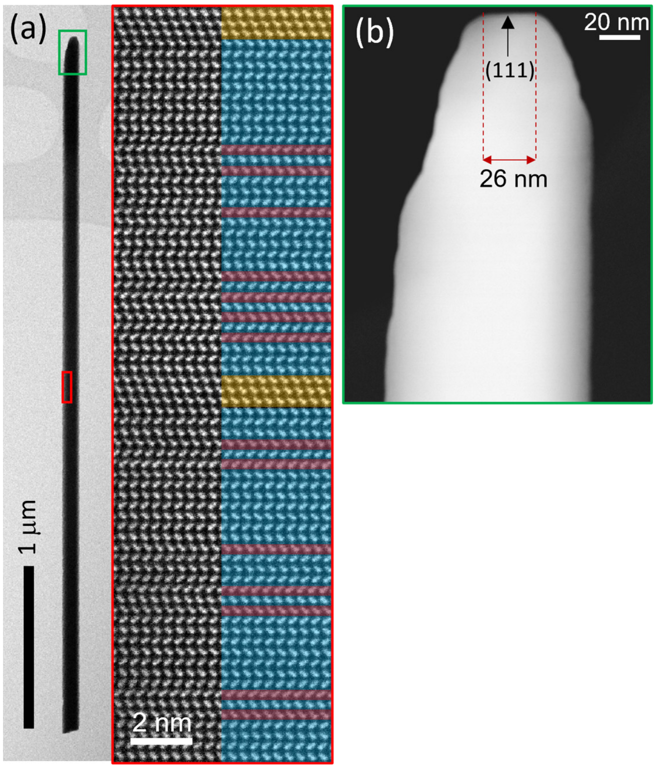

FIG. 2. (a) High magnification annular dark field (ADF) image of a nanowire from growth run C showing the typical crystal structure of the Te-doped nanowires. WZ regions containing stacking faults are marked in blue and red, respectively, and ZB inclusions are marked in yellow. The region used for the magnified image is indicated in the inset bright field (BF) low magnification image. (b) Higher magnification ADF image of the tip region. It appears to consist of multiple facets with the top (111) facet being smaller in diameter (≈26 nm) compared to the nanowire.

C. Atom probe tomography

For APT, single InAs nanowires with different Te-doping levels and a GaSb shell are isolated using a method described in detail in Ref. [42]. They are analyzed in a LEAP4000X HR equipment. We imaged the distribution of Te in the InAs nanowires utilizing the same methods for noise level suppression and background correction as in Ref. [42]. The APT analyses reveal four notable findings. First, as can be seen in Fig. 3, Te accumulates at the core of the wire and at the corners of the hexagonal {110} facets for all investigated Te-doping concentrations. Second, the measured Te-dopant incorporation increases with the corresponding nominal doping (cf. Figs. 3 and 4). Third, the Te concentration increases towards the bottom of the nanowires typically reaching a factor of 2–3 higher concentration near the bottom with respect to the top (cf. Fig. 4). Fourth, as depicted in Fig. 5, with the increase of Te nominal doping, the facets of the hexagonal InAs nanowires become unstable and the nanowires with the

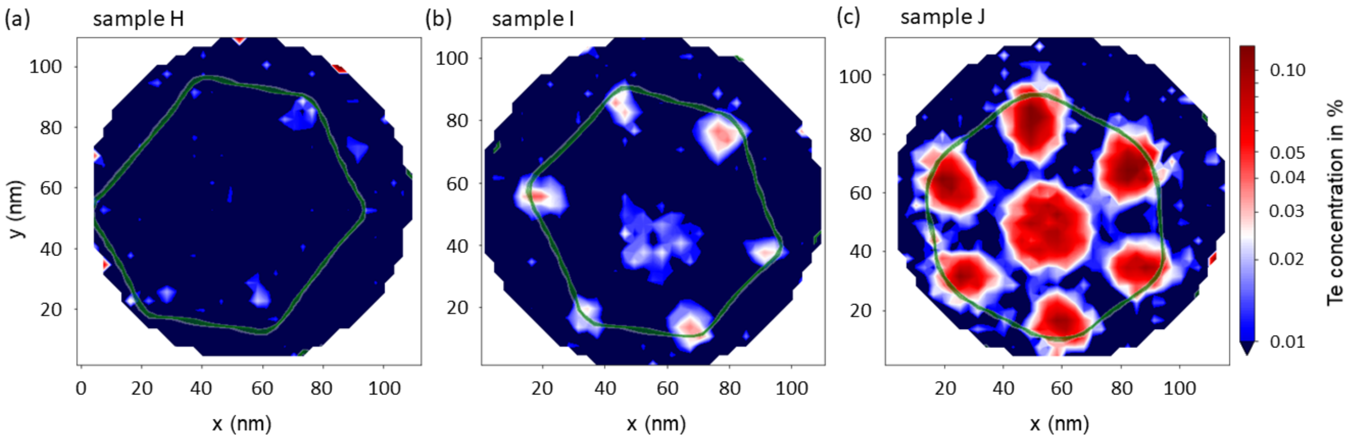

FIG. 3. Two-dimensional map of the Te concentration determined by APT from samples of growth runs H (a), I (b), and J(c).

highest doping have locally dodecagonal cross sections. This observation is confirmed by TEM cross sectional images, as shown in Supplemental Material Fig. S1 [44]. For the dodecagonal cross section the sixfold symmetry observed in the Te doping remains (cf. Supplemental Material Fig. S2 [44]).

We interpret these findings as follows. Te diffuses along the sidewall of the nanowire, a contribution coming also from the substrate surface, and incorporates via the small (111) growth facet on the top of the nanowire [Fig. 2(b)] and on the corners of the hexagonal facets. Note that the diameters of the top (111) facet in Fig. 2(b) and the Te-rich core in Fig. 3(c) are comparable. As the wire grows, the diffusion contribution of the substrate surface disappears and Te incorporation at the top decreases. Due to the large covalent radius of Te atoms, they accumulate on the corners between facets. The accumulation at the corners promotes the formation of (112) facets and hence the dodecagonal segments. One can presume that the surfactant Te incorporates easier into the solid on (111) and (112) surfaces than (110). Interestingly, a modulation of dopant incorporation was also found for Be-doped GaAs nanowires, but with a threefold symmetry [45].

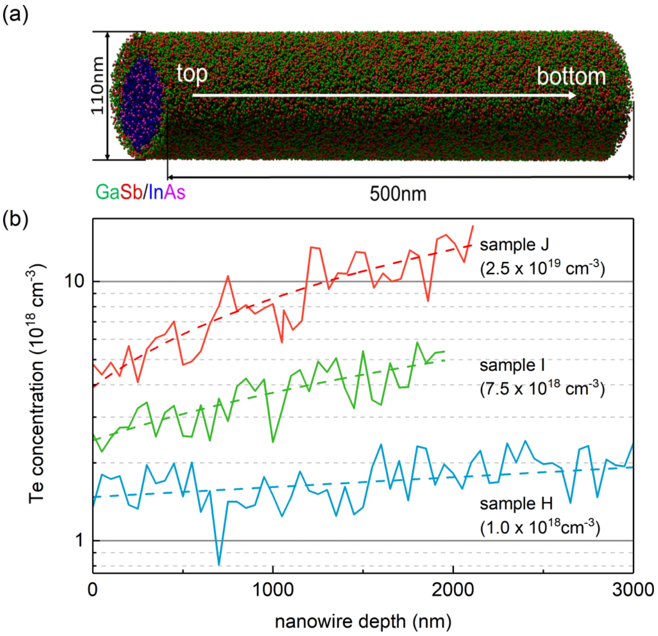

FIG. 4. (a) APT 3D map of an exemplary InAs/GaSb core/shell nanowire. The elements are displayed with different colors. (b) Axial atomic Te concentration profiles of samples from growth runs H, I, and J. The nominal Te-doping concentration is given in brackets.

D. Electrical characterization

In Fig. 6 the resistance at room temperature from nanowires with different doping levels are plotted functions of the ratio of nominal distance between the contacts and the cross sectional area d_{nom}/S. Here, S was determined for each growth series by averaging the diameters of the measured nanowires assuming a regular hexagonal shape. The transport measurements have been carried out in a four-terminal scheme in order to eliminate the effect of contact resistances. For each growth run with a specific doping concentration, one finds a linear increase of resistance with the contact separation length verifying the ohmic behavior of the transport in the wire. The doping effect of Te is confirmed by the decrease of the slope, i.e., decreased resistivity ρ, with increased doping concentration (cf. Table I). In Fig. 6 one observes that there is a spread of the resistance of different nanowires with identical contact separation. The effect is less pronounced for higher doping levels. One reason for the varying conductance could be found in nonuniform cross section S. Although the nanowires were grown in a selective-area epitaxy scheme, fluctuations of the cross sectional area cannot be excluded.

Charge carrier concentrations of nanowires with different doping levels were extracted from field-effect measurements by biasing a global back gate. We found that the conductance is reduced for negative gate voltages, confirming the n-type doping character. Quantitative information about charge carrier concentration was obtained using the threshold voltage V_{th} at pinch-off. Since nanowires with a Te-doping concentration larger than 5×10^{18} cm^{-3} did not reach pinch-off at accessible back-gate voltages, V_{th} was in this case obtained by extrapolating the approximately linear dependence towards positive voltages. Examples of traces including a linear fit are given in the Supplemental Material in Figs. S3– S5 [44]. Some nanowire samples showed a gate hysteresis behavior, which was reproducible during several cycles. In that case, V_{th} was determined by taking the average of the threshold voltages

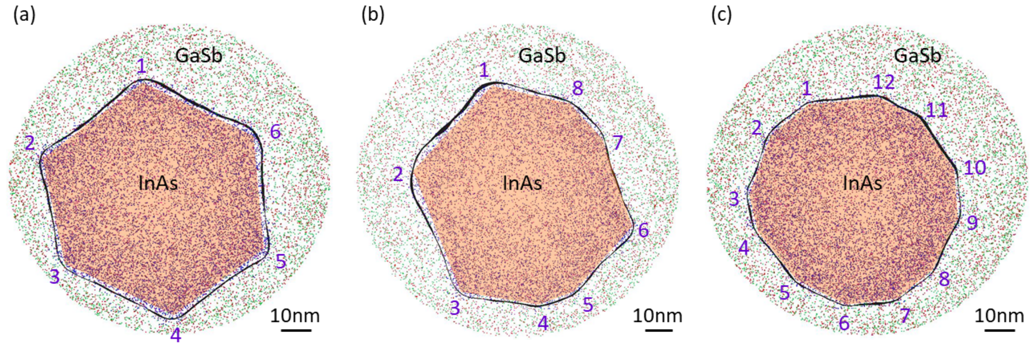

hexagonal	two extra facets	dodecagonal

FIG. 5. Cross section of InAs nanowires with different doping as obtained from 10 nm slices of APT measurements. The shape of the core is marked using 40% indium isoconcentration surfaces [43] and facets/corners are then marked manually. (a) Wires with low doping concentration (growth run H) always show hexagonal facets. (b) As the doping increases (growth run I) extra facets start appearing locally. (c) In highly doped samples (growth run J), there are sections with length of hundreds of nanometers which have dodecagonal shape.

for up and down sweeps. Details of the determination of V_{th} and the calculation of the charge carrier concentration n_{3D} are given in the Supplemental Material [44].

The field-effect measurements on nanowires grown with different Te-doping concentrations were carried out at room temperature and at 4.2 K. The corresponding charge carrier concentrations at different nominal doping concentrations are depicted in Fig. 7. The graphs confirm that the experimentally determined charge carrier concentration values increase with the nominal doping of the nanowires.

At the lowest Te-doping concentrations (samples A and B), the measured carrier concentration is somewhat higher than the nominal one. This might be due to the additional contribution of the surface accumulation layer [21]. For samples C and D, one finds that, at room temperature, the measured carrier concentrations are close to the nominal Te-doping concentrations demonstrating the efficient dopant incorporation. However, for samples E and F grown with the low As_4 flux, the doping efficiency is somewhat lower, the obtained charge carrier concentrations being lower than expected from the previous growth runs A to D. This could be explained by a modified Te incorporation due to altered growth conditions by decreased As_4 flux. The measured charge carrier concentrations are found to be generally higher at room temperature compared with 4.2 K, which represents the expected behavior in semiconductors.

A relatively large spread of n_{3D} for the investigated nanowires from identical batches is observed. A possible explanation for that is the imprecise character of the method to determine the charge carrier concentration from the gate pinch-off threshold voltage. Defects within the oxide and at the interface with the semiconductor effectively alter the capacitance used to determine the carrier concentration (see Sec. III B in the Supplemental Material [44]) leading to scattered results. Furthermore, it was shown in Fig. 4 that the Te incorporation along the nanowire axis is not uniform,

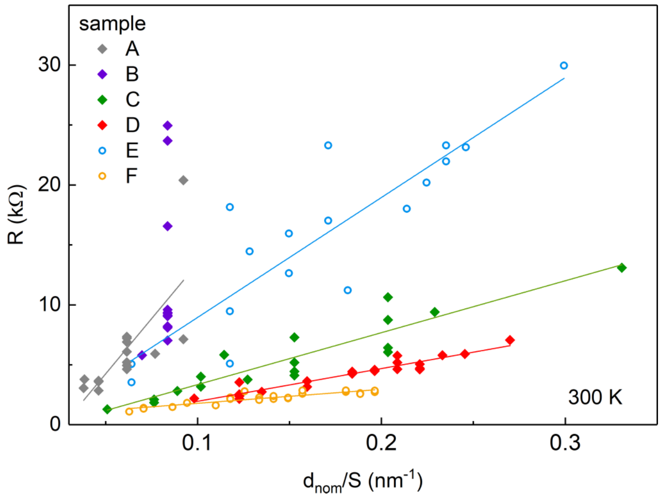

FIG. 6. Four-terminal resistance R of doped nanowires at room temperature plotted as a function of the ratio between nominal contact distance d_{nom} and mean nanowire cross sectional area S. The solid lines represent the linear fits to determine the resistivity. For the samples of growth run B no reliable linear fit was possible.

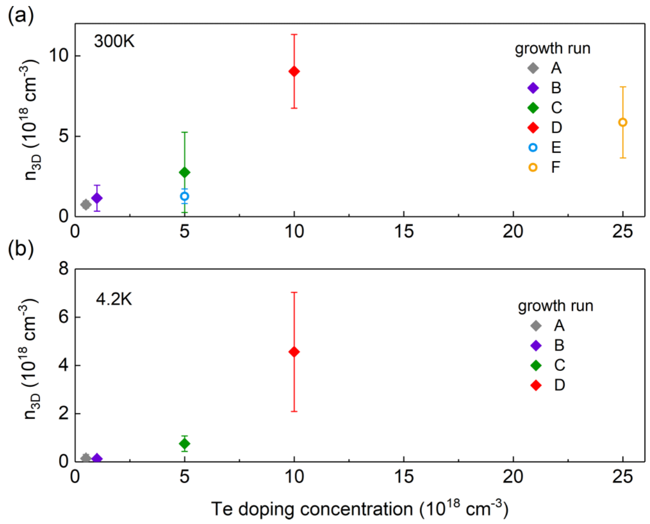

FIG. 7. (a) Extracted charge carrier concentrations n_{3D} from gate pinch-off curves at room temperature for nanowires with different nominal Te-doping concentrations (growth runs A to F). (b) n_{3D} at 4.2 K for growth runs A to D.

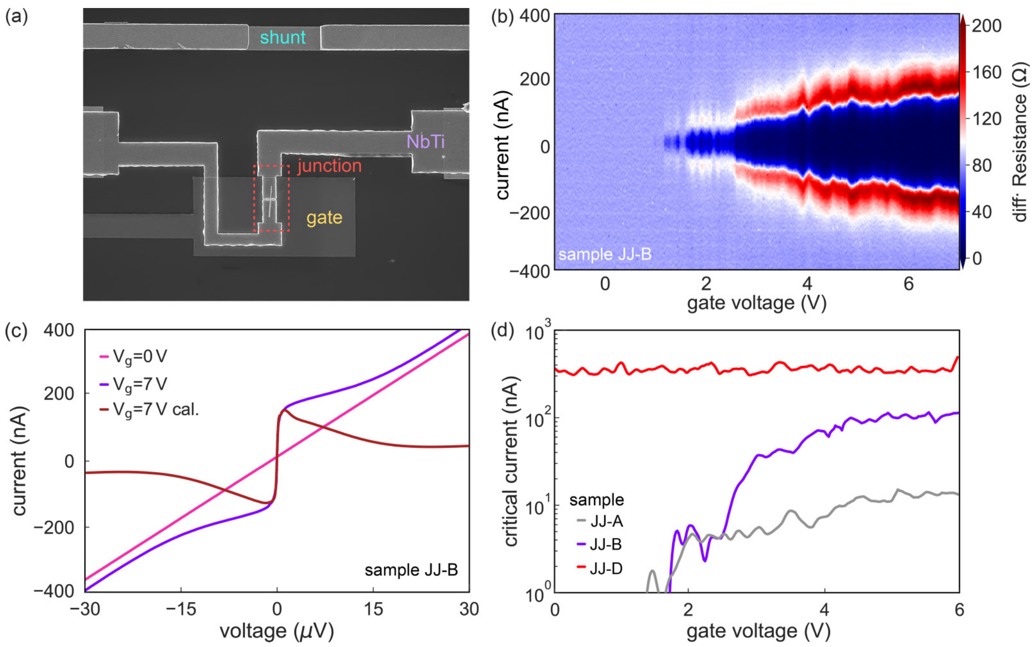

FIG. 8. (a) SEM micrograph of a nanowire Josephson junction that is connected in parallel to an extrinsic on-chip shunt resistor. The superconducting leads consist of a 80-nm-thick NbTi layer. The electrostatic tuning is realized by means of a global bottom gate pad. (b) Gate- and current-dependent differential resistance map of a nanowire Josephson junction of growth run B. The measurements were taken at 15 mK. (c) Single voltage-current characteristics taken from (a) at gate voltages of $V_g = 0$ V and 7 V. The calibrated characteristics for $V_g = 7$ V after subtracting the conductance of the shunt is also given. (d) Gate-dependent critical current for junctions JJ-A, JJ-B, and JJ-D at 15 mK.

resulting in different effective doping depending on the length of the particular nanowire. The current preparation scheme of the contact fingers did not allow us to measure specific sections along the nanowire. Therefore, one must be careful to directly compare the obtained results with measurements from APT. However, it can be concluded that the charge carrier concentration strongly depends on the nominal dopant concentration, suggesting an effective *n*-type doping of InAs by Te.

Field-effect mobilities at room temperature for growth runs A–F are given in Table I. Values found lie in comparable order of magnitude with previous Si-doped InAs nanowires [21]. However, no clear trend with doping concentration was found. Nanowires from growth runs A–D grown under similar conditions show a peak mobility at doping concentration 5×10^{18} cm^{-3}, decreasing again at higher doping.

E. Josephson junctions

In order to demonstrate the suitability of Te-doped nanowires for superconducting hybrid structures the properties of gate-controlled Josephson junctions are investigated. The measurements have been performed in a ^{3}He/^{4}He dilution refrigerator with a base temperature of 15 mK. The measured junctions JJ-A, JJ-B, and JJ-D were fabricated from nanowires from growth series A, B, and D, respectively. A typical structure is shown in Fig. 8(a), in which the nanowire-based Josephson junction is shunted by an AuGe resistor. The shunt was included to suppress hysteretic effects in the current-voltage characteristics and to improve the performance of the device in measurements of the ac-Josephson effect [46,47]. In Fig. 8(b) the color-coded differential resistance vs bias current is plotted in the gate voltage range from $V_g = -1$ V to 7 V for junction JJ-B made from a nanowire having a nominal doping concentration of 1×10^{18} cm^{-3}. One finds that for gate voltages below 1 V the nanowire is pinched-off, with the remaining resistance of 80 Ω given by the shunt resistor. Compared to the samples with ohmic contacts discussed in the previous section, the pinch-off is found at a larger gate voltage, which can be attributed to the different gate configuration, i.e., different gate dielectric and contact metallization. Between V_g=1 V and 2.5 V the device shows signatures of Coulomb blockade which can be attributed to the presence of an intrinsic quantum dot [48]. At gate voltages above 2.5 V, the nanowire channel is open and exhibits gate-tunable supercurrent, i.e., an important requirement for hybrid superconducting circuit applications. The critical current shows some superimposed fluctuations due to interference effects [13,14]. From Fig. 8(c) showing a single voltage-current ($I - V$) trace at $V_g = 7$ V (red curve) a critical current of $I_c = 140$ nA is extracted. The $I - V$ characteristics contain the contribution of the shunt resistor, which needs to be subtracted to gain the actual current through the junction. Indeed, the resistance of the shunt can be determined directly from the measurement at zero gate voltage [cf. Fig. 8(c)], where the junction is pinched-off completely. After the calibration of the junction response by means of a pointwise combination of the traces at 7 V and 0 V, it is possible to extract the unperturbed characteristics of the device [cf. Fig. 8(c), dark red trace]. Junctions JJ-A and JJ-B could be pinched-off completely so that the normal state resistance R_N could be extracted. At a gate bias of 7 V we determined I_cR_N

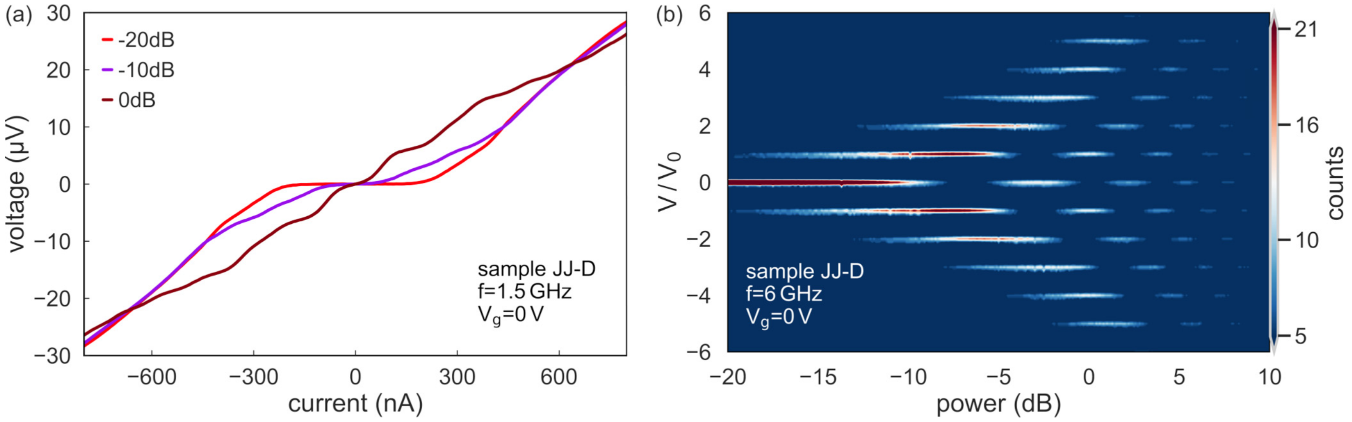

FIG. 9. (a) Current-voltage characteristics of junction JJ-D for different microwave powers. (b) Measurements of Shapiro steps as a function of power. The color scale corresponds to the number of measurement points at normalized voltages V/V_0 with $V_0 = hf/(2e)$.

products of 65 μV and 188 μV for samples JJ-A and JJ-B, respectively.

The critical current as a function of gate voltage for all investigated Josephson junctions are shown in Fig. 8(d). The junction containing a nanowire with the highest doping level only shows a weak relation between V_g and the measured I_c. In contrast, the wires with the lower carrier concentrations exhibit a transistorlike behavior with pronounced pinch-off and saturation regions. All critical currents show some fluctuations due to inference effects in the nanowire channel [13,14]. The difference in the threshold voltage between junctions JJ-A and JJ-B are attributed to Coulomb resonances which dominate the transport at low gate values [48]. A comparison of the critical current at $V_g = 6$ V reveals increase by a factor of 10 between JJ-A and JJ-B and a factor of 5 between JJ-B and JJ-D, which confirms the impact of the doping concentration on I_c.

A reliable way to confirm that nanowire-based junctions do indeed carry a Josephson supercurrent is to perform measurements under microwave irradiation. Here, the application of a microwave signal results in Shapiro steps of height $n \cdot V_0$, with $V_0 = hf/(2e)$, h Planck constant, and $n = 1, 2, 3, \ldots$. Figure 9(a) shows a set of current-voltage traces of junction JJ-D for $f = 5$ GHz and different microwave powers at $V_g = 7$ V. At low power, i.e., -20 dB, the curve basically mimics the behavior of a purely dc-driven junction. However, if the power is increased to -10 dB and further to 0 dB, the zero voltage state is gradually suppressed and equidistant voltage plateaus, i.e., Shapiro steps, appear. In Fig. 9(b) the presence of Shapiro steps at multiples of V_0 for $f = 6$ GHz is shown as a function of microwave power. The color scale gives the number of counts as a function of voltage, i.e., large number of counts corresponds to the appearance of a step. The regular oscillating pattern without any subharmonic features indicates a sinusoidal current-phase relation of the Josephson junction.

IV. CONCLUSIONS

We demonstrate that Te is an efficient dopant for MBE-grown InAs nanowires. At very high dopant concentrations, above 1×10^{19} cm^{-3}, a change in wire morphology was observed, where the hexagonal cross section changes to a dodecagonal one. The side facets have also a great influence on the distribution of the Te dopant, which accumulates at the corners of the hexagonal facets, as APT revealed. In addition, the APT showed that in the center of the wire the Te concentration is higher and that the total Te concentration increases toward the bottom of the nanowire. The effective doping was confirmed by electrical measurements at room temperature and 4 K, where a systematic increase in the conductivity of the wire with the doping concentration was observed. Indeed, a significant increase in the critical current was obtained in Josephson junctions with a nanowire weak link. At moderate doping concentrations, even gate control was maintained. Since InAs nanowires are often used in hybrid structures for Majorana physics or quantum computing, Te doping provides a very efficient method to tailor the nanowire properties for devices in these applications.

ACKNOWLEDGMENTS

We thank T. Ziegler, P. Liebisch, P. Pilch, B. Aarts, and A. Espiari for their assistance during sample preparation and M. Schleenvoigt for the metal deposition, M. Jansen for initial assistance with TEM, and B. Bennemann, C. Krause, and H. Kertz for technical assistance. Dr. F. Lentz and Dr. S. Trellenkamp are gratefully acknowledged for electron beam lithography and Dr. E. Neumann and S. Bunte for their assistance with the focused ion beam setup and scanning electron microscopy. Dr. G. Catelani is gratefully acknowledged for theory support regarding the magnetic field measurements. All samples have been prepared at the Helmholtz Nano Facility [49]. The work at Forschungszentrum Jülich was partly supported by the project "Scalable solid state quantum computing," financed by the Initiative and Networking Fund of the Helmholtz Association, by the Deutsche Forschungsgemeinschaft (DFG, German Research Foundation) Project "Coupling of quantum dots with superconductors" (SCHA 835/9-1). UK EPSRC is acknowledged for funding through Grant No. EP/P000916/1. The APT work was supported by NSERC Canada (Discovery, SPG, and CRD Grants), Canada Research Chairs, Canada Foundation for Innovation, Mitacs, PRIMA Québec, and Defence Canada [Innovation for Defence Excellence and Security (IDEaS)]. The work at RIKEN was partially supported by a Grant-in-Aid for Scientific Research (B) (No. 19H02548), Grants-in-Aid for Scientific Research (S) (No. 19H05610), Scientific Research on Innovative Areas "Science of hybrid quantum systems" (Grant No. 15H05867), and by Fujitsu Limited.

[1] S. Dayeh, D. P. Aplin, X. Zhou, P. K. Yu, E. Yu, and D. Wang, Small **3**, 326 (2007).
[2] K. Tomioka, P. Mohan, J. Noborisaka, S. Hara, J. Motohisa, and T. Fukui, J. Cryst. Growth **298**, 644 (2007).
[3] C. Thelander, C. Rehnstedt, L. E. Froberg, E. Lind, T. Martensson, P. Caroff, T. Lowgren, B. J. Ohlsson, L. Samuelson, and L.-E. Wernersson, IEEE Trans. Electron Devices **55**, 3030 (2008).
[4] A. M. Burke, D. J. Carrad, J. G. Gluschke, K. Storm, S. Fahlvik Svensson, H. Linke, L. Samuelson, and A. P. Micolich, Nano Lett. **15**, 2836 (2015).
[5] C. Fasth, A. Fuhrer, M. T. Bjork, and L. Samuelson, Nanoletters **5**, 1487 (2005).
[6] A. Fuhrer, L. E. Fröberg, J. N. Pedersen, M. W. Larsson, A. Wacker, M.-E. Pistol, and L. Samuelson, Nano Lett. **7**, 243 (2007).
[7] S. Heedt, A. Manolescu, G. A. Nemnes, W. Prost, J. Schubert, D. Grützmacher, and T. Schäpers, Nano Lett. **16**, 4569 (2016).
[8] S. Heedt, N. Traverso Ziani, F. Crépin, W. Prost, St. Trellenkamp, J. Schubert, D. Grützmacher, B. Trauzettel, and Th. Schäpers, Nat. Phys. **13**, 563 (2017).
[9] A. Iorio, M. Rocci, L. Bours, M. Carrega, V. Zannier, L. Sorba, S. Roddaro, F. Giazotto, and E. Strambini, Nano Lett. **19**, 652 (2019).
[10] A. Bordoloi, V. Zannier, L. Sorba, C. Schönenberger, and A. Baumgartner, Commun. Phys. **3**, 135 (2020).
[11] V. Mourik, K. Zuo, S. M. Frolov, S. R. Plissard, E. P. A. M. Bakkers, and L. P. Kouwenhoven, Science **336**, 1003 (2012).
[12] R. Aguado, Riv. Nuovo Cimento **40**, 523 (2017).
[13] Y.-J. Doh, J. A. van Dam, A. L. Roest, E. P. A. M. Bakkers, L. P. Kouwenhoven, and S. D. Franceschi, Science **309**, 272 (2005).
[14] H. Y. Günel, I. E. Batov, H. Hardtdegen, K. Sladek, A. Winden, K. Weis, G. Panaitov, D. Grützmacher, and T. Schäpers, J. Appl. Phys. **112**, 034316 (2012).
[15] T. W. Larsen, K. D. Petersson, F. Kuemmeth, T. S. Jespersen, P. Krogstrup, J. Nygård, and C. M. Marcus, Phys. Rev. Lett. **115**, 127001 (2015).
[16] G. de Lange, B. van Heck, A. Bruno, D. J. van Woerkom, A. Geresdi, S. R. Plissard, E. P. A. M. Bakkers, A. R. Akhmerov, and L. DiCarlo, Phys. Rev. Lett. **115**, 127002 (2015).
[17] A. Zazunov, V. S. Shumeiko, E. N. Bratus, J. Lantz, and G. Wendin, Phys. Rev. Lett. **90**, 087003 (2003).
[18] H. H. Wieder, Appl. Phys. Lett. **25**, 206 (1974).
[19] D. Razmadze, E. C. T. O'Farrell, P. Krogstrup, and C. M. Marcus, Phys. Rev. Lett. **125**, 116803 (2020).
[20] K. Sladek, V. Klinger, J. Wensorra, M. Akabori, H. Hardtdegen, and D. Grützmacher, J. Cryst. Growth **312**, 635 (2010).
[21] S. Wirths, K. Weis, A. Winden, K. Sladek, C. Volk, S. Alagha, T. E. Weirich, M. von der Ahe, H. Hardtdegen, H. Lüth, N. Demarina, D. Grützmacher, and T. Schäpers, J. Appl. Phys. **110**, 053709 (2011).
[22] H. Ghoneim, P. Mensch, H. Schmid, C. D. Bessire, R. Rhyner, A. Schenk, C. Rettner, S. Karg, K. E. Moselund, H. Riel, and M. T. Björk, Nanotechnology **23**, 505708 (2012).
[23] E. Dimakis, M. Ramsteiner, C.-N. Huang, A. Trampert, A. Davydok, A. Biermanns, U. Pietsch, H. Riechert, and L. Geelhaar, Appl. Phys. Lett. **103**, 143121 (2013).
[24] D. W. Park, S. G. Jeon, C.-R. Lee, S. J. Lee, J. Y. Song, J. O. Kim, S. K. Noh, J.-Y. Leem, and J. S. Kim, Sci. Rep. **5**, 16652 (2015).
[25] R. Sankaran, J. Cryst. Growth **50**, 859 (1980).
[26] M. Kamp, G. Mörsch, J. Gräber, and H. Lüth, J. Appl. Phys. **76**, 1974 (1994).
[27] B. R. Bennett, R. Magno, and N. Papanicolaou, J. Cryst. Growth **251**, 532 (2003).
[28] J. Wallentin and M. T. Borgström, J. Mater. Res. **26**, 2142 (2011).
[29] M. Orrù, E. Repiso, S. Carapezzi, A. Henning, S. Roddaro, A. Franciosi, Y. Rosenwaks, A. Cavallini, F. Martelli, and S. Rubini, Adv. Funct. Mater. **26**, 2836 (2016).
[30] N. I. Goktas, E. M. Fiordaliso, and R. R. LaPierre, Nanotechnology **29**, 234001 (2018).
[31] T. Hakkarainen, M. Rizzo Piton, E. M. Fiordaliso, E. D. Leshchenko, S. Koelling, J. Bettini, H. Vinicius Avanço Galeti, E. Koivusalo, Y. G. a. Gobato, A. de Giovanni Rodrigues, D. Lupo, P. M. Koenraad, E. R. Leite, V. G. Dubrovskii, and M. Guina, Phys. Rev. Materials **3**, 086001 (2019).
[32] N. A. Güsken, T. Rieger, G. Mussler, M. I. Lepsa, and D. Grützmacher, Nanoscale Res. Lett. **14**, 179 (2019).
[33] G. Koblmüller, S. Hertenberger, K. Vizbaras, M. Bichler, F. Bao, J.-P. Zhang, and G. Abstreiter, Nanotechnology **21**, 365602 (2010).
[34] P. Perla, H. A. Fonseka, P. Zellekens, R. Deacon, Y. Han, J. Kölzer, T. Mörstedt, B. Bennemann, A. Espiari, K. Ishibashi, D. Grützmacher, A. M. Sanchez, M. I. Lepsa and T. Schäpers, Nanoscale Adv. **3**, 1413 (2021).
[35] T. Rieger, D. Grützmacher, and M. I. Lepsa, Phys. Status Solidi RRL **7**, 840 (2013).
[36] No value of ρ for sample B was provided, because working samples were only available at one distance d_{nom}, so that no linear fit could be performed.
[37] R. Wixom, L. Rieth, and G. Stringfellow, J. Cryst. Growth **269**, 276 (2004).
[38] G. A. M. Sáfar, W. N. Rodrigues, L. A. Cury, H. Chacham, M. V. B. Moreira, S. L. S. Freire, and A. G. de Oliveira, Appl. Phys. Lett. **71**, 521 (1997).
[39] B. R. A. Neves, M. S. Andrade, W. N. Rodrigues, G. A. M. Sáfar, M. V. B. Moreira, and A. G. de Oliveira, Appl. Phys. Lett. **72**, 1712 (1998).
[40] E. Anyebe, M. K. Rajpalke, T. D. Veal, C. Jin, Z. Wang, and Q. Zhuang, Nano Res. **8**, 1309 (2015).
[41] H. Potts, M. Friedl, F. Amaduzzi, K. Tang, G. Tütüncüoglu, F. Matteini, E. Alarcon Lladó, P. C. McIntyre, and A. Fontcuberta i Morral, Nano Lett. **16**, 637 (2016).
[42] S. Koelling, A. Li, A. Cavalli, S. Assali, D. Car, S. Gazibegovic, E. P. A. M. Bakkers, and P. M. Koenraad, Nano Lett. **17**, 599 (2017).

[43] O. C. Hellman, J. B. du Rivage, and D. N. Seidman, Ultramicroscopy **95**, 199 (2003).

[44] See Supplemental Material at http://link.aps.org/supplemental/10.1103/PhysRevMaterials.6.024602 for additional material on transmission electron microscopy, atom probe tomography, determination of carrier concentration, and extrinsically shunted Josephson junctions.

[45] M. Dastjerdi, E. M. Fiordaliso, E. Leshchenko, A. Akhtari-Zavareh, T. Kasama, M. Aagesen, V. Dubrovskii, and R. LaPierre, Nano Lett. **17**, 5875 (2017).

[46] P. Joyez, D. Vion, M. Götz, M. Devoret, and D. Esteve, J. Supercond. **12**, 757 (1999).

[47] M. Chauvin, The Josephson effect in atomic contacts, Ph.D. thesis, Université Pierre et Marie Curie-Paris VI, 2005.

[48] P. Zellekens, R. Deacon, P. Perla, H. A. Fonseka, T. Mörstedt, S. A. Hindmarsh, B. Bennemann, F. Lentz, M. I. Lepsa, A. M. Sanchez, D. Grützmacher, K. Ishibashi, and T. Schäpers, Phys. Rev. Appl. **14**, 054019 (2020).

[49] Forschungszentrum Jülich GmbH, J. Large-Scale Facilities **3**, A112 (2017).